Electron energy-loss spectrum and exciton band structure of WSe_2 monolayer studied by *ab initio* Bethe-Salpeter equation calculations

Yun-Chen Shih, Fredrik Andreas Nilsson, 2, * and Guang-Yu Guo^{1,3,†}

¹Department of Physics and Center for Theoretical Physics, National Taiwan University, Taipei 10617, Taiwan

²CAMD, Computational Atomic-Scale Materials Design, Department of Physics,

Technical University of Denmark, 2800, Kgs. Lyngby, Denmark

³Physics Division, National Center for Theoretical Sciences, Taipei 10617, Taiwan

(Dated: July 23, 2024)

Bounded excitons in transition metal dichalcogenides monolayers lead to numerous opto-electronic applications, which require a detailed understanding of the exciton dynamics. The dynamical properties of excitons with finite momentum transfer Q can be investigated experimentally using electron energy-loss (EEL) spectroscopy. The EEL spectrum depends on the response function of the material which in turn is determined by the exciton energies and eigenvectors in the exciton band structure. In this work, we utilize ab initio density-functional theory plus Bethe-Salpeter equation (DFT+BSE) approach to explore the exciton band structure and also Q-resolved EEL spectrum in monolayer WSe₂. In particular, we carefully examine the discrepancies and connections among the existing EEL spectrum formulas for quasi-two-dimensional (2D) systems, and establish a proper definition of the EEL spectrum, which is then used to calculate the EEL spectra of monolayer WSe₂. We find that remarkably, the dispersion of the calculated lowest-energy EELS peaks for the in-plane momentum transfer follows almost precisely the non-parabolic upper band of the lowest bright A exciton, and also agrees well with the previous experiment. Furthermore, we show that only the bright exciton with its electric dipole being parallel to the direction of the transfered momentum is excited, i.e., EEL spectroscopy selectively probes bright exciton bands. This explains why only the upper band of the A exciton, which is a longitudinal exciton with an in-plane dipole moment, was observed in the previous experiment. Our findings will stimulate further EEL experiments to measure other branches of the exciton band structure, such as the parabolic lower band of the A exciton, and hence will lead to a better understanding of the exciton dynamics in quasi-2D materials.

I. INTRODUCTION

Atomically thin quasi-two-dimensional (quasi-2D) materials, such as transition metal dichalcogenides (TMDs) monolayers, have received significant attention due to their exceptional physical properties. The combination of the strong spin-orbit coupling (SOC) effect [1–3] and the broken inversion symmetry in the TMDs monolayers leads to the coupling between spin and valley degrees of freedom, and thus the valley dependent optical selection rules [4-8]. Moreover, due to the weak dielectric screening [9–12] and the geometric confinement [13], the enhanced Coulomb interaction between the electrons and holes in the TMDs monolayers gives rise to the formation of the strongly bound excitons with exceptionally large binding energies [11, 14–17] and huge oscillator strengths [18, 19], leading to the promising opto-electronic and photonic applications [20, 21].

Despite the violation of the momentum conservation rule in optical experiments, finite momentum excitons play the important roles as the de-excitation channels, significantly influence the photoluminescence and other time-dependent phenomena [22, 23]. This has driven investigations into finite momentum excitons over the past few years [24–29]. For the TMDs monolayers, the

excitation energies of the lowest bright excitons centered around the K and K' valleys are degenerate due to the time-reversal symmetry as $\mathbf{Q} \to 0$ [25]. Remarkably, as demonstrated by the theoretical calculations [24–26, 28, 30], the dispersions of the lowest bright excitons split into two bands, with the lower band showing a parabolic dispersion, while the upper band exhibits a strong non-parabolic dispersion. The different dispersion behaviors can give rise to the different emission properties such as exciton lifetimes and angular-dependent emission behaviors [28].

Electron energy-loss (EEL) spectroscopy (EELS) is a powerful technique to probe plasmons [31–34] and excitons with finite momenta [29, 33, 35]. In momentumresolved EELS in transmission geometry the measured spectrum represents the differential cross-section of the inelastic electron scattering for a given momentum transfer Q of the incident electrons [36]. The EEL spectrum provides information of the dynamical response of the materials, such as the plasmonic excitations [31, 32, 34, 37], the strong excitonic effects [29, 34, 35, 38], and the localized plasmon-exciton coupling [33]. The theoretical studies [33–35] investigating the excitonic effects on the EEL spectra using Bethe-Salpeter equation (BSE) calculations primarily focus on the optical limit ($\mathbf{Q} \to 0$). However, in practice, the experimental measurements can never reach exactly $\mathbf{Q} \to 0$ [35, 39]. Therefore, the theoretical analysis of the excitonic effects on the EEL spectra at non-vanishing Q is required. In this work, we per-

^{*} fanni@dtu.dk

[†] gyguo@phys.ntu.edu.tw

form the state-of-the-art ab initio BSE calculations and present a comprehensive study of the significant excitonic effects on the EEL spectra in the finite \mathbf{Q} regime.

Conventionally, the EEL spectrum is defined as the inverse of the momentum- and energy-resolved macroscopic dielectric function $(\varepsilon_M(\mathbf{Q},\omega))$ as $L(\mathbf{Q},\omega) =$ $-\text{Im}[1/\varepsilon_{\text{M}}(\mathbf{Q},\omega)]$ [36, 40]. While this quantity is welldefined for three-dimensional (3D) bulk systems, for quasi-2D systems ε_M is significantly influenced by the supercell volume adopted in periodic calculations. This has led to confusion about how to correctly calculate the EEL spectrum in 2D materials, with fundamentally different definitions used in different works [33, 35, 36, 40, 41]. Therefore we begin by examining the most commonly used definitions of the EEL spectrum for quasi-2D systems, elaborate on the connections between these formulas, and provide a well-defined, easily implementable EEL spectrum formula for quasi-2D systems, suitable for the momentum and energy regimes studied in this work. We then focus on monolayer WSe₂ and analyse its EEL spectrum and exciton band structure, and also compare the calculated EEL spectrum with the recent experiment [29]. Similar to that reported by Qiu et al. [25] for monolayer MoS₂ and by Sauer et al. [28] for the MoS₂, MoSe₂, WS₂, and WSe₂ monolayers, we find that the lowest-energy A exciton branches split, with the lower branch displaying parabolic behavior and the upper branch exhibiting non-parabolic behavior. We show that the EELS peaks unambiguously follow the non-parabolic upper band and thus has a linear dependence on Q, indicating a direct connection of the dispersion relations of the EELS peaks to the exciton band structure. We also find that EEL spectroscopy selectively probes only the bright exciton bands with their electric dipole being parallel to the direction of the transfered momentum. This explains why only the upper band of the A exciton, which is a longitudinal exciton with an in-plane dipole moment, was observed in the previous experiment [29].

This paper is organized as follows. In Sec. II, we briefly introduce the central theories of ab initio quasiparticle and exciton band structure calculations, followed by the computational details adopted in this work. In Sec. III. we carry out a thorough analysis of the widely used definitions of the EEL spectrum for quasi-2D systems, highlight the connections among these formulas, and provide a properly defined EEL spectrum formula for quasi-2D systems for the momentum and energy regimes studied in this work. In Sec. IV, we present the main results of the application of the theoretical methods outlined in Sec. II and Sec. III, covering the electronic and optical properties of monolayer WSe₂, as discussed in Sec. IV A. In Sec. IV B, we discuss the exciton band structures in the small but finite Q regime. In Sec. IV C, we present the calculated EEL spectra and examine the dispersion of the peaks in the EEL spectrum, and we discuss the exciton excitation mechanism by EELS. Finally, we summarize the results of this work in Sec. V.

II. AB INITIO BETHE-SALPETER EQUATION CALCULATION

All calculations were performed with the electronic structure code GPAW [42–45] using the accurate grid-based projector augmented-wave method (PAW) [45].

A. Structural relaxations

For the structural relaxations we used density functional theory (DFT) within the generalized gradient approximation (GGA) with the Perdew-Burke-Ernzerhof (PBE) exchange-correlation functional [46]. For the optimizer we use the BFGS algorithm [44]. We model the WSe₂ monolayer using the slab supercell method, employing a vacuum thickness of 15 Å. We use a $24 \times 24 \times 1$ Γ -centered k-mesh sampling over the 2D Brillouin zone (BZ) and a plane-wave cutoff of 500 eV.

B. G_0W_0 quasi-particle calculations

The present G_0W_0 quasi-particle (QP) calculations are performed by using the GPAW code [42, 47]. The QP energies $E_{n\mathbf{k}}^{\mathrm{QP}}$ are evaluated perturbatively by the linearized QP equation

$$E_{n\mathbf{k}}^{\mathrm{QP}} = E_{n\mathbf{k}}^{\mathrm{KS}} + Z_{n\mathbf{k}} \langle \psi_{n\mathbf{k}}^{\mathrm{KS}} | \Sigma_{\mathrm{GW}} + v_x - v_{xc} | \psi_{n\mathbf{k}}^{\mathrm{KS}} \rangle \qquad (1)$$

where $E_{n\mathbf{k}}^{\mathrm{KS}}$ and $\psi_{n\mathbf{k}}^{\mathrm{KS}}$ are the Kohn-Sham eigen-energies and wave functions. $Z_{n\mathbf{k}}$ is the QP weight. Σ , v_x , and v_{xc} are the GW self-energy, non-local exchange potential, and local exchange-correlation potential, respectively [47, 48].

In the G_0W_0 calculation, we adopt a k-mesh of $24 \times 24 \times 1$, 1200 bands, and a dielectric cutoff energy of 250 eV. We utilize 2D truncated Coulomb interactions [11, 12] between the WSe₂ monolayer and its periodic replica. This approach is combined with the analytical treatment around the Γ -point to achieve faster k-points convergence when evaluating the screened interaction [48]. The G_0W_0 self-energy is computed using the full frequency integration.

C. The Bethe-Salpeter equation at finite momentum transfer

The Bethe-Salpeter equation (BSE) describing the exciton with the center-of-mass momentum \mathbf{Q} reads [49, 50]

$$(E_{c\mathbf{k}+\mathbf{Q}}^{\mathrm{QP}} - E_{v\mathbf{k}}^{\mathrm{QP}})A_{vc\mathbf{k}}^{\lambda,\mathbf{Q}} + \sum_{v'c'\mathbf{k}'} \langle vc\mathbf{k}\mathbf{Q}|K^{eh}|v'c'\mathbf{k}'\mathbf{Q}\rangle A_{v'c'\mathbf{k}'}^{\lambda,\mathbf{Q}}$$

$$= \Omega^{\lambda}(\mathbf{Q})A_{vc\mathbf{k}}^{\lambda,\mathbf{Q}}$$
(2)

where $E_{c\mathbf{k}+\mathbf{Q}}^{\mathrm{QP}} - E_{v\mathbf{k}}^{\mathrm{QP}}$ is the excitation energy of a free electron-hole pair, with the hole belonging to the band

with index v and the electron to the band with index c, forming a pair-orbital. $\Omega^{\lambda}(\mathbf{Q})$ is the momentum-resolved exciton excitation energy of the λ -th state, and the corresponding exciton state can be expressed as the linear combination of the pair-orbitals with the expansion coefficients $A_{vc\mathbf{k}}^{\lambda,\mathbf{Q}}$, and the absolute square of the expansion coefficients, referred to as the exciton weight, represents the contributions of the pair-orbitals to the exciton wave function in reciprocal space. The electron-hole interaction is $K^{eh} = K^x + K^d$. Here K^x is the exchange bare Coulomb term [49, 50]

$$\langle vc\mathbf{k}\mathbf{Q}|K^{x}|v'c'\mathbf{k}'\mathbf{Q}\rangle = \sum_{\mathbf{G}} \rho_{vc\mathbf{k}}^{*}(\mathbf{Q}, \mathbf{G})v_{\mathbf{G}}(\mathbf{Q})\rho_{v'c'\mathbf{k}'}(\mathbf{Q}, \mathbf{G}).$$
(3)

 K^d is the direct screened Coulomb term [49, 50]

$$\langle vc\mathbf{k}\mathbf{Q}|K^d|v'c'\mathbf{k}'\mathbf{Q}\rangle = -\sum_{\mathbf{G}\mathbf{G}'} \rho_{cc'\mathbf{k}+\mathbf{Q}}^*(\mathbf{q},\mathbf{G})W_{\mathbf{G}\mathbf{G}'}(\mathbf{q})\rho_{vv'\mathbf{k}}(\mathbf{q},\mathbf{G}')$$
(4)

where $\rho_{vc\mathbf{k}}(\mathbf{Q}, \mathbf{G}) = \langle v\mathbf{k}|e^{-i(\mathbf{Q}+\mathbf{G})\cdot\mathbf{r}}|c\mathbf{k}+\mathbf{Q}\rangle$ is the pair density, \mathbf{G} is the reciprocal lattice vector, and $\mathbf{q} = \mathbf{k} - \mathbf{k}'$. $v_{\mathbf{G}}(\mathbf{Q})$ and $W_{\mathbf{G}\mathbf{G}'}(\mathbf{q})$ are the bare Coulomb potential and the screened Coulomb potential in reciprocal space, respectively.

In the Tamm-Dancoff approximation (TDA), we construct the density response function in reciprocal space as [50, 51]

$$\chi_{\mathbf{G}\mathbf{G}'}(\mathbf{Q},\omega) =$$

$$\frac{1}{V_c} \sum_{\lambda} \sum_{v c \mathbf{k}} \sum_{v' c' \mathbf{k}'} \frac{A_{v c \mathbf{k}}^{\lambda, \mathbf{Q}} \rho_{v c \mathbf{k}}(\mathbf{Q}, \mathbf{G}) \left[A_{v' c' \mathbf{k}'}^{\lambda, \mathbf{Q}} \rho_{v' c' \mathbf{k}'}(\mathbf{Q}, \mathbf{G}') \right]^*}{\omega - \Omega^{\lambda}(\mathbf{Q}) + i\eta}$$
(5)

where V_c is the cell volume.

The exciton can be categorized into two distinct types—longitudinal and transverse excitons—depending on how its center-of-mass momentum aligns with its dipole matrix element [52]. The dipole matrix element of an exciton state $|\lambda\rangle$ is defined as

$$\mathbf{P}_{\lambda} = \sum_{vc\mathbf{k}} A_{vc\mathbf{k}}^{\lambda,\mathbf{Q}} \frac{\langle v\mathbf{k} | \mathbf{p} | c\mathbf{k} + \mathbf{Q} \rangle}{E_{c\mathbf{k}+\mathbf{Q}}^{\mathrm{QP}} - E_{v\mathbf{k}}^{\mathrm{QP}}}$$
(6)

where **p** is the momentum operator. A longitudinal exciton refers to the case when the dipole matrix element aligns with the center-of-mass momentum **Q**, while for a transverse exciton they are perpendicular to each other [52]. At $\mathbf{Q} \to 0$, Eq. (6) represents the oscillator strength of an exciton state $|\lambda\rangle$ that constitutes the optical absorption spectrum [49].

Our BSE calculations were performed on top of the DFT band structure and we shift the DFT band gap to match the G_0W_0 band gap at the high-symmetric K point. We included 4 top valence bands and 4 lowest conduction bands to construct the BSE matrix, and the

2D truncated Coulomb interaction is used to avoid the spurious screening from the periodic images of the monolayer. The electronic screening was calculated using 100 bands with a dielectric cutoff of 50 eV. A dense k-mesh of $72 \times 72 \times 1$ is adapted for both the ground state and BSE calculations to achieve the high resolution in momentum transfer for the \mathbf{Q} -dependent EEL spectra.

III. THEORY OF ELECTRON ENERGY LOSS SPECTRA OF QUASI-2D MATERIALS

A. Optical absorbance

The macroscopic dielectric function $(\varepsilon_M(\mathbf{Q}, \omega))$ is the key quantity to obtain the optical properties of a 3D bulk system, which is evaluated as [51]

$$\varepsilon_M(\mathbf{Q}, \omega) = \frac{1}{\varepsilon_{\mathbf{G}\mathbf{G}'}^{-1}(\mathbf{Q}, \omega)\big|_{\mathbf{G}=0, \mathbf{G}'=0}}$$
(7)

where $\varepsilon_{\mathbf{G}\mathbf{G}'}(\mathbf{Q},\omega)$ is the dielectric matrix in reciprocal space, which related to $\chi_{\mathbf{G}\mathbf{G}'}(\mathbf{Q},\omega)$ as

$$\varepsilon_{\mathbf{GG'}}^{-1}(\mathbf{Q},\omega) = 1 + v_{\mathbf{G}}(\mathbf{Q})\chi_{\mathbf{GG'}}(\mathbf{Q},\omega).$$
 (8)

Inverting the dielectric matrix is necessary to include the local field effects [51]. However, it is cumbersome to evaluate all the dielectric matrix elements and perform the matrix inversion. Alternatively, we can obtain $\varepsilon_M(\mathbf{Q},\omega)$ as [51]

$$\varepsilon_M(\mathbf{Q}, \omega) = 1 - v_0(\mathbf{Q})\bar{\chi}_{00}(\mathbf{Q}, \omega)$$
 (9)

where $\bar{\chi}_{\mathbf{G}\mathbf{G}'}(\mathbf{Q},\omega)$ is the modified density response function in reciprocal space [50, 51]. Within the BSE formalism, $\bar{\chi}_{\mathbf{G}\mathbf{G}'}(\mathbf{Q},\omega)$ has the same structure as $\chi_{\mathbf{G}\mathbf{G}'}(\mathbf{Q},\omega)$ (see Eq. (5)), but the exciton eigenvectors and eigenvalues are obtained by using the modified BSE kernel [50, 51], which adopts the modified bare Coulomb interaction $\bar{v}_{\mathbf{G}}$ [51]

$$\bar{v}_{\mathbf{G}}(\mathbf{Q}) = \begin{cases} 0 & \text{(if } \mathbf{G} = 0) \\ v_{\mathbf{G}}(\mathbf{Q}) & \text{(else)} \end{cases}$$
 (10)

For a quasi-2D system, a thick vacuum spacing between periodic quasi-2D systems has to be adopted in the supercell calculations to eliminate the spurious interlayer interaction. However, because $\bar{\chi}_{00}$ is proportional to the inverse of V_c [50], with the increasing vacuum thickness, $\varepsilon_M(\mathbf{Q},\omega)$ in Eq. (9) will tend to unity, indicating the physical properties of a quasi-2D system will be overwhelmed by that of the vacuum layer. To be able to reduce the size of the supercell in the z-direction, a truncated Coulomb interaction can be used [53]. In 3D bulk materials, the bare Coulomb interaction $v_{\mathbf{G}}(\mathbf{Q}) = 4\pi/|\mathbf{Q} + \mathbf{G}|^2$. In quasi-2D materials, we

replace $v_{\mathbf{G}}(\mathbf{Q})$ with the truncated Coulomb interaction $v_{\mathbf{G}}^{trunc}(\mathbf{Q})$, which is given by [53, 54]

$$v_{\mathbf{G}}^{trunc}(\mathbf{Q}) = \frac{4\pi}{|\mathbf{Q} + \mathbf{G}|^2} [1 - e^{-|\mathbf{Q}_{||} + \mathbf{G}_{||}|d/2} \cos(G_z d/2)]$$
(11)

where d is the length of the supercell in the non-periodic direction, and the truncation length is set to d/2. However, since $v_0^{trunc}(\mathbf{Q} \to 0) \approx 2\pi d/|\mathbf{Q}|$, a straightforward use of Eq. (9) would also result in a vanishing absorption spectra. Therefore, we define the polarizability as [10, 42]

$$\alpha(\omega) = -\lim_{|\mathbf{Q}| \to 0} \frac{d}{|\mathbf{Q}|^2} \bar{\chi}_{\mathbf{00}}(\mathbf{Q}, \omega). \tag{12}$$

If a truncated Coulomb interaction is used to evaluate $\bar{\chi}_{00}(\mathbf{Q},\omega)$, this polarizability remains finite even a thick vacuum is adopted. Equation (12) measures the induced dipole momentum per area of a quasi-2D system [10, 42]. The imaginary part of the polarizability represents the optical absorbance [10, 42].

B. Electron energy-loss spectrum

1. Different EEL spectrum formulas

The momentum-dependent EEL spectrum is obtained experimentally through transmission electron energy-loss spectroscopy [29, 39]. The quantity that is directly measured in the electron energy-loss spectroscopy experiments is the doubly differential cross-section $(\partial^2 \sigma/\partial\Omega\partial\omega)$ [40], which represents the relative probability for the incident electron experiencing a scattering into the solid angle $(d\Omega)$ and energy interval $(\omega \to \omega + d\omega)$. The doubly differential cross section is [55]

$$\frac{\partial^2 \sigma}{\partial \Omega \partial \omega} = (\frac{\partial \sigma}{\partial \Omega})_{Ruth} S(\mathbf{Q}, \omega) \tag{13}$$

where \mathbf{Q} is the total momentum transfer of an incident electron. The doubly differential cross-section is the product of two terms. The first term $(\partial \sigma/\partial \Omega)_{Ruth} = 4/(a_B|\mathbf{Q}|^4)$ is the elastic Rutherford scattering cross-section, where a_B is the Bohr radius. This term describes the elastic differential cross-section of two charged particles, with the interaction between them being the Coulomb force. The other term $S(\mathbf{Q}, \omega)$ is the dynamical structure factor, containing the information on the response of the electrons in the system to the external perturbation [55]. $S(\mathbf{Q}, \omega)$ in 3D is related to the inverse dielectric function in reciprocal space as [36]

$$S(\mathbf{Q}, \omega) \equiv -\frac{|\mathbf{Q}|^2}{4\pi^2 e^2} \text{Im}[\varepsilon_{00}^{-1}(\mathbf{Q}, \omega)]. \tag{14}$$

Since $S(\mathbf{Q}, \omega) \sim |\mathbf{Q}|^2$ for small \mathbf{Q} , we define the EEL spectrum $(L(\mathbf{Q}, \omega))$ as the dimensionless quantity

$$L(\mathbf{Q}, \omega) = \frac{4\pi^2 e^2}{|\mathbf{Q}|^2} S(\mathbf{Q}, \omega) \equiv -\text{Im}[\varepsilon_{00}^{-1}(\mathbf{Q}, \omega)].$$
 (15)

However, from the discussion of the absorption spectra in the previous section, it is evident that a straightforward calculation of EEL spectrum from the dielectric function will give a vanishing EEL spectrum as $\mathbf{Q} \to 0$ in quasi-2D materials. There are different strategies to solve this problem in the literature, which yield different definitions of the EEL spectrum. The two most commonly used definitions are listed as $Definition\ 1$ and $Definition\ 2$ below.

Definition 1: The EEL spectrum is conventionally obtained from taking the imaginary part of the inverse of the macroscopic dielectric function $(\varepsilon_M(\mathbf{Q}, \omega))$ analogously to the 3D case [36, 40]

$$L(\mathbf{Q}, \omega) = -\text{Im}[1/\varepsilon_{M}(\mathbf{Q}, \omega)]$$

$$= \frac{\text{Im}[\varepsilon_{M}(\mathbf{Q}, \omega)]}{(\text{Re}[\varepsilon_{M}(\mathbf{Q}, \omega)])^{2} + (\text{Im}[\varepsilon_{M}(\mathbf{Q}, \omega)])^{2}}.$$
(16)

This definition of EEL spectrum is equivalent to the 3D formula in Eq. (15), and it has been widely used also for quasi-2D materials in the literature [32, 35, 56–58]. However, as discussed above $\varepsilon_M \to 1$ for large supercells, or even for finite supecells if a truncated Coulomb interaction is used to evaluate the dielectric matrix. Therefore, this formula can only be used without Coulomb truncation and for finite supercells and is in principle not applicable to quasi-2D systems. get a reasonable definition in quasi-2D systems, one can evaluate ε_M from Eq. (9) where $\bar{\chi}_{00}$ is evaluated with a truncated Coulomb interaction. However, the matrix inversion formula used to derive Eq. (9) relies on the assumption that the Coulomb interaction used to calculate $\chi_{\mathbf{GG}'}(\mathbf{Q})$ in Eq. (8) is the same as the $v_0(\mathbf{Q})$ in the product $(v_0(\mathbf{Q})\bar{\chi}_{00}(\mathbf{Q},\omega))$. Using a untruncated interaction $v_0(\mathbf{Q}) = 4\pi/|\mathbf{Q}|^2$ but a truncated interaction $v^{trunc}_{\mathbf{G}}(\mathbf{Q})$ to evaluate $\chi_{\mathbf{G}\mathbf{G}'}(\mathbf{Q})$ is thus an approximation which, as we will see, has a relatively large impact on the results. When we refer to Definition 1 below, we will always consider the case where ε_M is evaluated from Eq. (9) and $\bar{\chi}$ is evaluated with a truncated Coulomb interaction. To avoid the scaling of the spectra with the supercell size, Liou et al. [32] introduced the effective volume approach by replacing the supercell volume with half of the bulk counterpart to calculate the EEL spectra of graphene.

Definition 2: The EEL spectrum has also been defined to be related to the imaginary part of the density response function $\chi_{00}(\mathbf{Q},\omega)$ as [33]

$$L(\mathbf{Q}, \omega) = -\frac{4\pi}{|\mathbf{Q}|^2} \text{Im} \chi_{\mathbf{00}}(\mathbf{Q}, \omega). \tag{17}$$

For 3D bulk systems, this definition is equivalent to Eqs. (15)-(16). For quasi-2D systems, despite $\chi_{00}(\mathbf{Q}, \omega) \propto 1/V_c$, we note that Eq. (17) does not suffer from the supercell size problem or the need to use an approximate matrix inversion formula (like *Definition 1* above) since

 χ can be directly evaluated with a truncated Coulomb interaction. On the other hand, to get a quantity which is independent of the supercell size, Eq. (17) can be multiplied by d, which is the size of the supercell in the z-direction (similar to the polarizability in the previous section)

$$\tilde{L}(\mathbf{Q}, \omega) = -\frac{4\pi d}{|\mathbf{Q}|^2} \text{Im} \chi_{\mathbf{00}}(\mathbf{Q}, \omega). \tag{18}$$

As will be shown in the following section, Eq. (18) can be formally derived as a limiting case of the integrated EELS formula proposed in Ref. [41]. However, since d is just an overall multiplicative factor, and the experimental spectra is typically normalized, the additional factor d is typically not important in practical calculations. Eq. 17 is implemented in the GPAW code [42], and has been adopted in the previous works on quasi-2D systems [31, 33, 37, 59].

Both definitions above rely on an analogy to the 3D case and only depends on the macroscopic components $(\mathbf{G} = \mathbf{G}' = 0)$ of the response functions. However, for quasi-2D systems which are confined in the z-direction it is not immediately clear that the finite G_z components should vanish. Actually, as shown in Ref. [41] and discussed under *Definition 3* below, all G_z components of χ contribute to the EEL spectrum.

Definition 3: Starting from Eq. (15) with an explicit dynamical structure factor S applicable to a quasi-2D system, Nazarov [41] showed that the relevant quantity for the doubly differential cross-section in EELS for quasi-2D materials is what we here will call the integrated EELS

$$\tilde{L}(\mathbf{Q},\omega) = -\frac{4\pi}{|\mathbf{Q}|^2} \operatorname{Im} \int_{-\infty}^{\infty} e^{iq_z(z'-z)} \chi_{\mathbf{00}}(z,z',\mathbf{Q}_{||},\omega) dz dz'$$
(19)

where \mathbf{Q} is the total momentum transfer of a incident electron consisting of its in-plane component $\mathbf{Q}_{||}$ and out-of-plane component $q_z \mathbf{\hat{z}}$. $\chi_{\mathbf{G}_{||}\mathbf{G}'_{||}}(z, z', \mathbf{Q}_{||}, \omega)$ is the in-plane Fourier transform of the density response function [60]. This formula is rigorous but difficult to implement.

In the following section, we will demonstrate that Eq. (19) proposed by Nazarov [41] will actually reduce to Eq. (18) within the energy and momentum-transfer regimes discussed in this article.

2. Justification for the EELS formula used in this work

To construct the formula of EEL spectrum for quasi-2D systems without relying on ε_M , tailored to fit the energy and momentum-transfer regimes discussed in this article, we start from the EEL spectrum formula proposed by

Nazarov [41] (Definition 3)

$$\tilde{L}(\mathbf{Q},\omega) = -\frac{4\pi}{|\mathbf{Q}|^2} \operatorname{Im} \int_{-\infty}^{\infty} e^{iq_z(z'-z)} \chi_{\mathbf{00}}(z,z',\mathbf{Q}_{||},\omega) dz dz'.$$
(20)

Firstly, $\chi_{\mathbf{G}_{||}\mathbf{G}'_{||}}(z, z', \mathbf{Q}_{||}, \omega)$ is related to the density response function in reciprocal space $\chi_{\mathbf{G}\mathbf{G}'}(\mathbf{Q}_{||}, \omega)$ as [60]

$$\chi_{\mathbf{G}_{||}\mathbf{G}_{||}'}(z, z', \mathbf{Q}_{||}, \omega) = \frac{1}{d} \sum_{G_z G_z'} e^{iG_z z} \chi_{\mathbf{G}\mathbf{G}'}(\mathbf{Q}_{||}, \omega) e^{-iG_z' z'}$$
(21)

where d is the length of the unit cell in the out-of-plane direction z. Next, the expression for q_z is [41]

$$q_z = \frac{\omega + \frac{\hbar}{2m} |\mathbf{Q}_{||}|^2}{v} \tag{22}$$

where v and m are the velocity and mass of the incident electron, respectively. In practice, $|\mathbf{Q}_{||}| \gg q_z$ due to the high velocity of the incident electrons [29, 39]. By exploiting the fact that $\chi_{\mathbf{G}_{||}\mathbf{G}'_{||}}(z,z',\mathbf{Q}_{||},\omega)$ would practically only be nonzero for -d/2 < z < d/2 and -d/2 < z' < d/2, we can relate $\tilde{L}(\mathbf{q},\omega)$ and $\chi_{\mathbf{G}\mathbf{G}'}(\mathbf{Q}_{||},\omega)$ via Eq. (19) and Eq. (21) as

$$\tilde{L}(\mathbf{Q}, \omega) = -\frac{4\pi}{|\mathbf{Q}|^2 d} \sum_{G_z G_z'} \operatorname{Im} \chi_{\mathbf{0} G_z \mathbf{0} G_z'}(\mathbf{Q}_{||}, \omega) \frac{2 - 2\cos(q_z d)}{(G_z - q_z)(G_z' - q_z)}.$$
(23)

Note that $q_z d$ is practically a small number because of the high velocity of the normally incident electrons [29, 39]. Consequently, performing the Taylor expansion of Eq. (23) up to the lowest order in \mathbf{Q} yields

$$\tilde{L}(\mathbf{Q}, \omega) = -\frac{4\pi d}{|\mathbf{Q}|^2} \operatorname{Im} \chi_{\mathbf{00}}(\mathbf{Q}_{||}, \omega) - \frac{4\pi d}{|\mathbf{Q}|^2} \sum_{G_z, G_z' \neq 0} \operatorname{Im} \chi_{\mathbf{0}G_z \mathbf{0}G_z'}(\mathbf{Q}_{||}, \omega) \frac{q_z^2}{(G_z - q_z)(G_z' - q_z)}.$$
(24)

The $G_z=G_z'=0$ component dominates the EEL spectrum, while the contributions of other $G_z\neq 0$ or $G_z'\neq 0$ terms in Eq. (24) are significantly smaller because $q_z\ll G_z$ and $q_z\ll G_z'$ in the energy and momentum transfer regions that we focus on in this work. As a result, within the limit of $q_z d\ll 1$ and noting that $|\mathbf{Q}_{||}|\gg q_z$, Eq. (19) reduces to

$$\tilde{L}(\mathbf{Q}_{||},\omega) = -\frac{4\pi d}{|\mathbf{Q}_{||}|^2} \operatorname{Im} \chi_{\mathbf{00}}(\mathbf{Q}_{||},\omega). \tag{25}$$

This formula is exactly the same as Eq. (18). Eqs. (17) and (18) has already been adopted in several previous papers on the quasi-2D systems [31, 33, 37, 59]. However, rather than motivating it from an analogy with the 3D case, we derive it from the rigorous formalism of EEL

spectrum (i.e., Eq. (19)). Our derivation shows that Definition~2 is valid in the low- ${\bf Q}$ region with the standard electron energies used in EELS. For the electron energies in Ref. [29], the upper bound of ${\bf Q}_{||}$ is ${\bf Q}_{||} \ll 8.8~{\rm \AA}^{-1}$ (see supplementary note 1 in the Supplemental Material (SM) [61]). For lower electron energies and higher ${\bf Q}$ the full formula (Definition~3) has to be used. Furthermore, the other commonly used formula Definition~1 cannot be derived in any rigorous manner and should therefore be considered as an ad~hoc procedure. As we will show below this ad~hoc formula also yields worse agreement with experiment.

It is worth noting that for a quasi-2D system, $\bar{\chi}_{00}(\mathbf{Q},\omega)$ is equivalent to $\chi_{00}(\mathbf{Q},\omega)$ as $\mathbf{Q} \to 0$ [33, 34]. Therefore, the optical absorbance has the same structure as the EEL spectrum [33, 34]. This is a unique characteristic of a quasi-2D system, as explained below. The $\mathbf{G} = 0$ component of the electron-hole exchange interaction K^x (Eq. 3) consists of the pair density $\rho_{vck}(\mathbf{Q}, \mathbf{0})$ and the Coulomb potential $v_0(\mathbf{Q})$. As $\mathbf{Q} \to 0$, $\rho_{vck}(\mathbf{Q}, \mathbf{0})$ is proportional to $|\mathbf{Q}|$ [37, 50] for both 3D bulk and quasi-2D systems. For quasi-2D systems, the Coulomb potential behaves as $v_0(\mathbf{Q}) \sim 1/|\mathbf{Q}|$ after applying Coulomb truncation [53, 54]. This implies that the $\mathbf{G} = 0$ term of K^x scales as $|\mathbf{Q}|$, making it negligible in the optical limit $(\mathbf{Q} \to 0)$. Consequently, the full BSE kernel is reduced to the modified BSE kernel [33, 34], indicating that $\bar{\chi}_{00}$ is equivalent to χ_{00} . This behavior is different for 3D bulk systems, where the Coulomb potential scales as $1/|\mathbf{Q}|^2$.

IV. APPLICATION TO WSE₂ MONOLAYER

We begin by presenting the GGA and G_0W_0 quasiparticle band structure of the WSe₂ monolayer to determine the effective masses and scissor shift. We then show the optical absorbance obtained within the scissorcorrected BSE (SC-BSE) framework, identifying five exciton states. Subsequently, we analyze the exciton band structures of the A exciton and its dark counterpart in the small \mathbf{Q} regime. Following this, we calculate the EEL spectra and present the dispersion curves of the EELS peaks. Finally, we discuss the exciton excitation mechanism in EELS to explain these dispersion curves.

A. Electronic and optical properties

Figure 1 shows the GGA and G_0W_0 quasi-particle band structures of the WSe₂ monolayer. Our GGA calculation indicates that the WSe₂ monolayer is a semi-conductor with the K - K direct band gap (E_{KK}) of 1.236 eV, which underestimates the experimental values (see Table I). In contrast, the G_0W_0 quasi-particle band gap exhibits a significant improvement and aligns well with the experimental values, indicating the importance of G_0W_0 quasi-particle calculations. In accordance with previous calculations [14, 68] as well as experimental

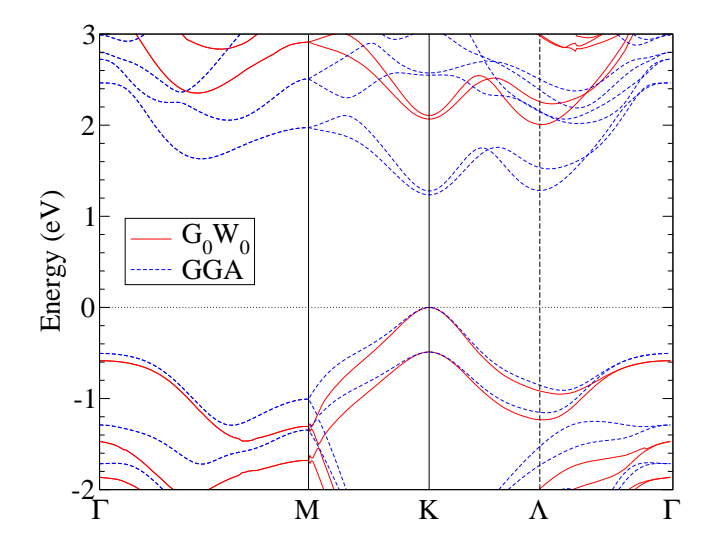


FIG. 1. Quasi-particle band structure of the WSe₂ monolayer from our G_0W_0 (solid red lines) and GGA (blue dashed lines) calculations. The valence band maximum, located at the K point, is shifted to 0 eV.

measurements [63], the G_0W_0 bandstructure reveals that the WSe₂ monolayer has a $K - \Lambda$ indirect quasi-particle band gap $(E_{K\Lambda})$ of 2.007 eV with the conduction band minimum at the Λ point lying midway between the Γ and K points. The difference between the K - K band gap and K – Λ band gap, defined as $\Delta_{K-\Lambda} = E_{K\Lambda} - E_{KK}$, is -60 meV, agrees well with the experimental measurements [63, 69] (see Table I). Additionally, the significant spin-orbit coupling (SOC) effect in the WSe₂ monolayer, attributed to the heavy tungsten element, leads to the substantial valence and conduction bands splitting of 488 meV and 39.5 meV at the K valleys. The SOC-induced valence band splitting is consistent with the experimental findings (see Table I), and the relatively small conduction band splittings are slightly larger than the experimental measurements. We also list the effective masses (in unit of free electron mass m_0) of the highest valence band (m_v) , lowest and second lowest conduction bands (labeled as m_{c_1} and m_{c_2}). The effective masses are obtained by fitting the electronic bands centered at the K point with a third-order polynomial. The fitting range spans $\mathbf{Q} = 0.05 \text{ Å}^{-1}$ (within 3 % of the size of Brillouin zone) in the Γ M direction. Notably, the differences between the effective masses obtained from the GGA and G_0W_0 band structures are small (within 1 % differences). In the following scissor-corrected Bethe-Salpeter equation (SC-BSE) calculations, we shift the GGA K – K direct band gap to align it with that of the G_0W_0 QP band structure. We find that the difference between the GGA+scissor and the G_0W_0 band structures in the vicinity of the K point is small, as shown in Fig. S5 of the SM [61], indicating the scissor correction is a good approximation for describing the exciton states centered around the K valleys.

Figure 2 illustrates the imaginary part of polarizabil-

TABLE I. The electronic band gaps at the K-K transition (E_{KK}) and K – Λ transition $(E_{K\Lambda})$. $\Delta_{K-\Lambda}$ is the energy difference between E_{KK} and $E_{K\Lambda}$ ($\Delta_{K-\Lambda} = E_{K\Lambda} - E_{KK}$). The SOC-induced energy splitting between the first two topmost valence bands (Δ_{SOC}^v) and the two lowest conduction bands (Δ_{SOC}^c) at the K point. The effective masses (in unit of free electron mass m_0) of the highest valence band (m_v) , lowest and the second lowest conduction bands $(m_{c_1}$ and m_{c_2}). The available experimental data (Expt.) are listed for comparison.

<u> </u>	E_{KK} (eV)	$E_{K\Lambda}$ (eV)	$\Delta_{K-\Lambda} \; (\mathrm{meV})$	$\Delta^{v}_{SOC} \; (\text{meV})$	$\Delta^c_{SOC} \; (\text{meV})$	$m_v (m_0)$	$m_{c_1} (m_0)$	$m_{c_2} (m_0)$
GGA	1.236	1.283	47	490	42.1	0.330	0.391	0.264
G_0W_0	2.067	2.007	-60	488	39.5	0.333	0.390	0.264
Expt.	$2.2^{\rm a},1.95^{\rm b}$	2.12^{a}	-80ª	$475^{\rm b}, 513^{\rm c}$	$14^{\rm d}, 12 \pm 0.5^{\rm e}$	$0.35^{\rm c}$		

^a Reference [63]

e Reference [67]

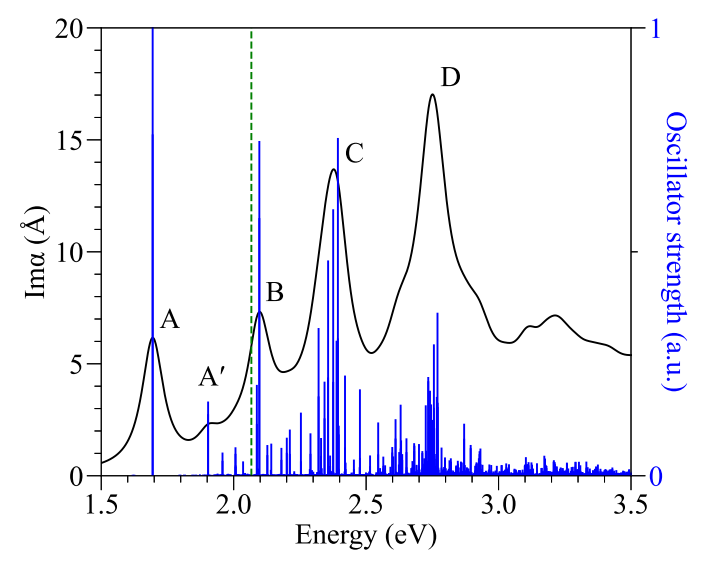


FIG. 2. The imaginary part of the polarizability of the WSe₂ monolayer calculated within the SC-BSE framework (solid black line) and the normalized oscillator strengths (blue vertical lines) of each exciton. The first four pronounced bright exciton peaks are labeled by A, B, C, and D. The peak with small intensity between the A and B peaks is labeled by A'. The dashed green line indicates the quasi-particle band gap.

ity of the WSe₂ monolayer calculated within the SC-BSE framework using Eq. (12) (black solid line) and the normalized oscillator strengths (blue vertical lines) of each exciton. The quasi-particle band gap is also shown (green dashed line). The strong excitonic effects of the WSe₂ monolayer significantly alter the absorption spectrum in the low-energy window. In the quasi-particle band gap, a prominent peak (labeled A) corresponds to the lowest-energy bright exciton state with the highest oscillator strength. Figure 3(b) illustrates the dominant weight of the A exciton on top of the spin-resolved DFT+scissor band structure. The A exciton originates from the pair-orbitals comprised of the topmost valence band and the second lowest conduction band having the same spin ori-

entation (like-spin transition states) and are located at the K and K' valleys. The reduced electronic screening effect in the WSe₂ monolayer results in the large binding energy of 0.374 eV which agrees well with the measured values (see TABLE II). The significant SOC-induced energy splitting between the first two highest valence bands introduces another bright exciton state labeled B, which contributes to the intense peak located slightly above the QP band gap. The dominant weight of the B exciton is primarily located at the like-spin transition between the second highest valence band and the lowest conduction band (see Fig. S6(a)). The large exciton excitation energy separation between the A and B excitons leads to the observation of the less intense peak (labeled A') between A and B peaks, corresponding to an exciton state in the QP band gap with the binding energies of 0.164 eV. The dominant weight of the A' exciton is primarily located at the same like-spin transition as the A exciton (see Fig. S6(b)). This indicates A' exciton is one of the excited states of the A exciton Rydberg series. Unlike the A, A', and B peaks, the high-energy C and D peaks consist of numerous exciton states with finite oscillator strength, resulting in the high spectrum intensity.

B. Exciton band structure

The excitation energy of an exciton Ω^{λ} depends on its center-of-mass momentum \mathbf{Q} , and the relation between Ω^{λ} and \mathbf{Q} is referred to as the exciton band structure, which contains essential information of the exciton dynamics. Figure 3(a) shows the two-dimensional hexagonal Brillouin zone of the WSe₂ monolayer with special points denoted by gray dots, and the blue (red) line that starts from the Γ point indicates \mathbf{Q} along Γ M (Γ K) direction. Since our emphasis is on the excitons that are localized around the K and K' points, as shown in Fig. 3(b), we further shift these arrows to the K and K' points to illustrate the corresponding transitions for a given \mathbf{Q} . Figure 4 illustrates the exciton band structure of the WSe₂ monolayer obtained by solving SC-BSE for the \mathbf{Q} along both Γ M and Γ K directions. The exciton excitation en

^b Reference [64]

c Reference 65

d Reference [66]

TABLE II. Exciton excitation energy $(\Omega(0))$ and exciton binding energy (E_b) for various bright exciton states of WSe₂ monolayer. The available experimental data (Expt.) are also listed for comparison.

	$\Omega(0) \; (eV)$	E_b (eV)		$\Omega(0) \text{ (eV)}$	
	Exciton A	(A')	Exciton B	Exciton C	Exciton D
SC-BSE	1.693 (1.903)	0.374 (0.164)	2.097	2.374	2.748
Expt.	$1.65^{\mathrm{a}}, \ 1.67^{\mathrm{b}}, \ 1.661^{\mathrm{c}}$	$0.37^{\rm a}, 0.315^{\rm b}$	$2.08^{a,b}$	2.43^{d}	$2.89^{\rm d}$

- a Reference [17]
- ^b Reference [70]
- c Reference 69
- d Reference [19]

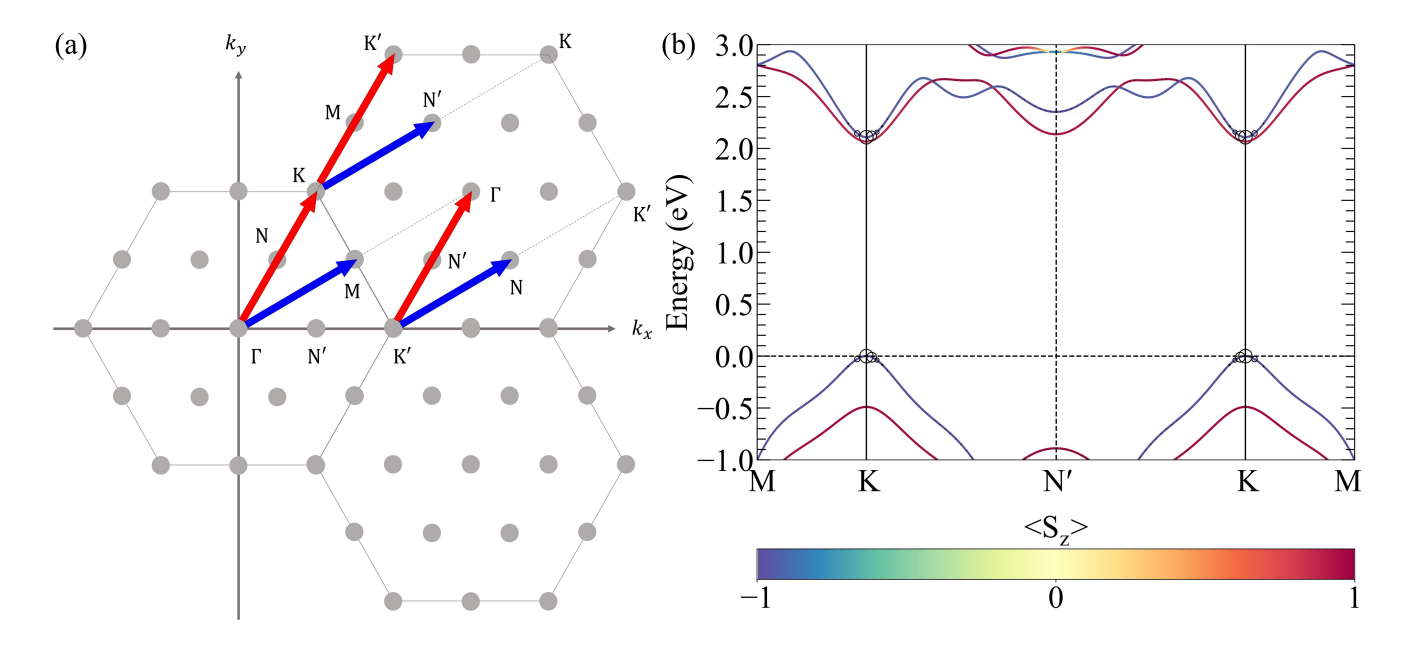


FIG. 3. (a) The two-dimensional hexagonal Brillouin zone. The special points are labeled, and they are denoted by gray dots. The blue and red arrows indicate the momentum transfers along ΓM and ΓK directions. These arrows are then shifted to the K and K' points, indicating the corresponding transitions for excitons that are localized at the K and K' points. (b) The spin-resolved DFT+scissor band structure spans from one K point to another, passing through the middle N point. Colors from blue to red represent the expectation value of spin projection in z direction, indicating the spin polarization. We also show the A exciton weight (black circles) of the pair-orbitals that have the dominant contributions.

ergies are black dots, and the gray dashed lines serve as a guide to the eye for a better visualization of the exciton band structure. The excitation energy of the A exciton at $\mathbf{Q} \to 0$ is indicated by the horizontal red line. The four lowest-energy exciton excitation energies correspond to the A exciton and its dark counterpart. We then present these four exciton bands with the fitting curves (blue lines). Following Ref. [25] (also see supplementary note 2 in the SM [61], we fit the two lowest dark excitons and the lower band of the A exciton to

$$\Omega(\mathbf{Q}) = \Omega(0) + A_2 |\mathbf{Q}|^2. \tag{26}$$

The upper band of the A exciton clearly demonstrates a non-parabolic behavior. Consequently, we fit it to a third-order polynomial, defined as

$$\Omega(\mathbf{Q}) = \Omega(0) + A_1 |\mathbf{Q}| + A_2 |\mathbf{Q}|^2 + A_3 |\mathbf{Q}|^3.$$
 (27)

We choose the direction of fitting to be ΓM , which has

more data points than ΓK , and the fitting range spans $\mathbf{Q} = 0.15 \text{ Å}^{-1}$ (about 8 % of the size of Brillouin zone). Remarkably, the excitation energies in the ΓK direction align closely with the fitting curves shown in Fig. 4, suggesting isotropy in the excitation energies of the A exciton and its dark counterpart.

At $\mathbf{Q} = 0$, the two lowest bright excitons responsible for the A resonance in Fig. 2 are energetically degenerate with the excitation energy of $\Omega(0)$, as required by time-reversal symmetry [25, 28]. On the other hand, we find that the two lowest dark excitons of the WSe₂ monolayer exhibit a small but nonzero energy splitting (4 meV), opposed to the MoS₂ monolayer where the lowest two spin-forbidden dark excitons remain degenerate [25, 30]. This behavior is consistent with the previous theoretical study [27], which presents the splitting of roughly 12 meV. In supplementary note 3 [61], we show that the dark exciton energy splitting converges with the in-

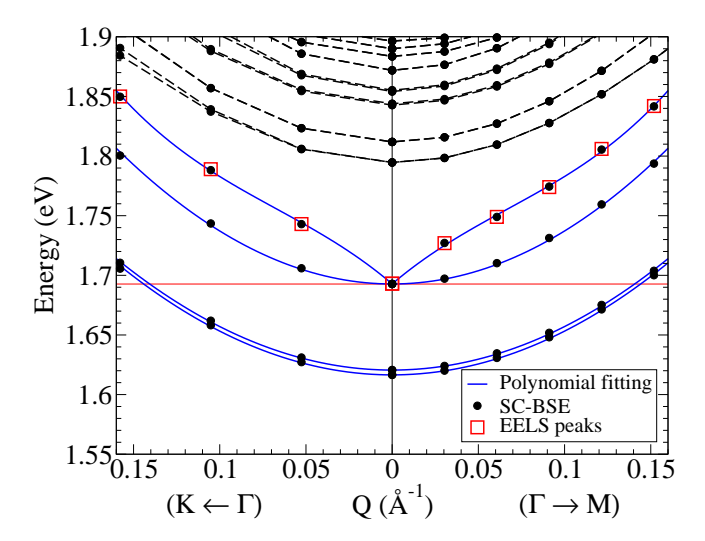


FIG. 4. The exciton band structure and the calculated EELS peaks dispersion of the A exciton of the WSe₂ monolayer. The black dots are the exciton excitation energies by solving SC-BSE at different \mathbf{Q} , and the red squares are the lowest A EELS peak positions. The four lowest exciton bands are represented by a polynomial fit in Γ M direction (blue lines), while the rest exciton excitation energies are connected by black dashed lines serving as a guide to the eye. The excitation energy of the A exciton states at $\mathbf{Q} = 0$ is indicated by the horizontal red line.

creasing vacuum thickness, indicating it is not caused by spurious interlayer interactions in supercell periodic calculations. Nevertheless, the underlying reason remains unclear. There are two main factors resulting in the excitation energy difference between the bright A exciton and its dark counterpart (denoted as Δ_{DA}). (i) The energy difference between the two lowest conduction bands is 42 meV (see Table I). (ii) The lowest conduction band exhibits a heavier effective mass compared to the second lowest conduction band, which gives rise to a greater exciton binding energy of the dark excitons than the bright excitons. These factors add up to an excitation energy splitting of 76 meV, which agrees well with the finding of a previous theoretical study [27] (see TABLE III).

At finite Q, the degeneracy of the two bright excitons is lifted due to the electron-hole exchange interaction [25, 28], and they develop into two branches. The lower bright exciton band shows a parabolic dispersion behavior. According to our polynomial fitting, we find the exciton effective mass of the lower band of the A exciton (denoted as M_{B1}) to be 0.857 m_0 , where m_0 is free electron mass, and its value agrees well with the previous theoretical study (see Table III). Note that M_{B1} is significantly enhanced compared to the total mass of the free electron-hole pair $M = m_v + m_{c_2}$ (roughly 0.594 m_0), this is due to the electron-hole interaction, including the direct and exchange terms [25]. On the other hand, the upper band of the A exciton does not exhibit a clear parabolic dispersion behavior in the small Q region (see Fig. 4). This non-parabolic behavior of the A exciton band is absent from the previous study by Deilmann $et\ al.\ [27]$. However, they adopted the 3D Coulomb potential in solving BSE without using the 2D truncated Coulomb interaction. In fact, according to the $\mathbf{Q} \cdot \mathbf{p}$ perturbation theory, and employing the fact that the two degenerate bright excitons are highly localized at the K and K' valleys, one can construct an effective BSE Hamiltonian in the tight-binding limit and diagonalize it to obtain the exciton band structure, as demonstrated by Qiu $et\ al.\ [25]$ and Sauer $et\ al.\ [28]$. For this effective Hamiltonian the lowest bright exciton bands will undergo a split, leading to the formation of the non-parabolic upper band (labeled $\Omega_l(\mathbf{Q})$)

$$\Omega_l(\mathbf{Q}) = \Omega(0) + 2A |\mathbf{Q}| + \left(\frac{\hbar^2}{2M} + \alpha + \beta + |\beta'|\right) |\mathbf{Q}|^2$$
(28)

and the parabolic lower band (labeled $\Omega_p(\mathbf{Q})$)

$$\Omega_p(\mathbf{Q}) = \Omega(0) + \left(\frac{\hbar^2}{2M} + \alpha + \beta - |\beta'|\right) |\mathbf{Q}|^2$$
 (29)

where $\Omega(0)$ is the exciton excitation energy at $\mathbf{Q} \to 0$, $M = m_e + m_h$ is the total mass of the effective masses of the electron and hole that primarily constitute the exciton. Here, A is the proportionality constant of the linear terms in the intravalley and intervalley exchange i interaction [25, 30], α is the proportionality constant from the Q^2 contribution from the direct term, β and β' are the Q^2 contribution from intravalley and intervalley exchange terms, respectively.

Due to the interplay of the long-range part (i.e. the $\mathbf{G}=0$ term) of the intravalley and intervalley exchange interaction [25, 30], the upper band of the A exciton has a linear term in \mathbf{Q} , which is absent from the lower band. It is this linear term that yields the energy splitting between the two branches at small \mathbf{Q} . Note that the linear term is a distinct signature of a quasi-2D system (i.e., adopting the 2D Coulomb potential), and it causes the non-parabolic behavior of the upper branch, as seen in our *ab initio* calculations and other theoretical studies [25, 28, 30].

The two lowest dark exciton bands, on the other hand, exhibit the parabolic dispersion behaviors, and the 4 meV energy separation observed at $\mathbf{Q}=0$ persists at finite \mathbf{Q} . Table III summarizes the exciton effective masses extracted from the fitting curves. The exciton effective masses of the two lowest dark excitons (denoted as M_{D1} and M_{D2}) are comparable, and they are significantly heavier than M_{B1} due to the following two factors. (i) The total mass of the free electron-hole pairs that comprise the dark exciton $M=m_v+m_{c_1}$ is heavier than that of the bright exciton $M=m_v+m_{c_2}$ since $m_{c_1}>m_{c_2}$. (ii) The difference between the intravalley and intervalley exchange interaction will further decrease M_{B1} [25], while both terms are absent from the dark excitons.

TABLE III. The energy difference between the bright A exciton and its dark counterpart (Δ_{DA}) . The exciton effective mass of the parabolic lower band of the bright exciton (M_{B1}) and the two lowest dark excitons (M_{D1}) and M_{D2} extracted from the fitting curves. The available theoretical values are listed.

	$\Delta_{DA} \; (\text{meV})$	M_{B1} (m_0)	M_{D1} (m_0)	M_{D2} (m_0)
SC-BSE	76	0.857	1.039	1.044
Theory	$70^{\rm a}$	$0.877^{\rm b}$		

^a Reference [27]

C. Electron energy-loss spectrum

1. Momentum-dependent EEL spectrum

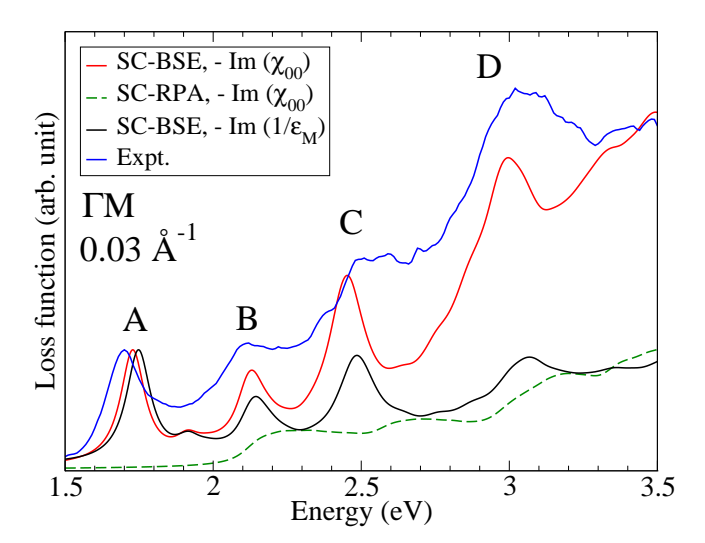


FIG. 5. The calculated momentum-dependent EEL spectra of the WSe₂ monolayer along Γ M direction for $Q=0.03~\text{Å}^{-1}$. Within the SC-RPA framework, we show the EEL spectrum obtained via Eq. (17) (green dashed line). Within the SC-BSE framework, we show the EEL spectra obtained via Eq. (17) (red solid line) and Eq. (16) (black solid line). The experimental EEL spectrum taken from Ref. [29] (blue solid line) is also shown for comparison. All the theoretical spectra have been normalized based on the experimental A exciton peak intensities. The first four pronounced EELS peaks are labeled by A, B, C, and D.

Figure 5 shows the experimental and calculated momentum-dependent EEL spectra of the WSe₂ monolayer along Γ M direction for Q=0.03 Å⁻¹. The experimental spectra is taken from Ref. [29]. First, we consider the two spectra evaluated using Eq. (17) (Definition 2) labelled Im(χ_{00}) in the figure. Within the scissor-corrected random phase approximation (SC-RPA) framework (green dashed line), the EEL spectrum fails to capture the main features of the experimental spectrum. This is because the strong excitonic effects dominate the

spectrum in the low-energy and small Q regimes presented in Fig. 5, and RPA framework omits the attractive electron-hole screened Coulomb interaction that is responsible for the formation of the excitons [51]. Remarkably, after including the excitonic effects by solving SC-BSE, the corresponding EEL spectrum (red solid line) captures the four distinct EELS peaks (labeled A, B, C, and D in Fig. 5), which agrees well with the experimental spectrum. Next, we consider the EEL spectrum that is determined using the inverse of the macroscopic dielectric function (Eq. (16)) (Definition 1) labelled $-\text{Im}(1/\varepsilon_M)$ in the figure. Here the macroscopic dielectric function is calculated within the SC-BSE framework using Eq. (9) and a truncated Coulomb interaction, and we have used the effective thickness to be half of the cell thickness of bulk WSe₂. The EEL spectrum calculated using Eq. (16) exhibits peaks at different positions and varying relative intensities compared to the EEL spectrum derived from Eq. (17). The latter demonstrates superior performance over the former when compared to the experimental spectrum. This sheds light on the importance of using the suitable formula of EEL spectrum, as we have discussed in Sec. III B.

Figures 6(a) and 6(b) illustrate the calculated EEL spectra of the WSe₂ monolayer compared to the experimental spectra taken from Ref. [29] along the Γ M and Γ K directions, respectively. At $\mathbf{Q} \to 0$, the theoretical EEL spectrum of the WSe₂ monolayer is the same as the optical absorbance (see Fig. S7(a)) as explained in Sec. III B. Alternatively, this can be understood as the fact that the Coulomb interaction in reciprocal space goes as 1/Q for the small momentum transfers in a two-dimensional system, which effectively turns off the long-range coupling between electrons, thereby curbs the formation of the plasmon [33, 34]. As shown in the SM [61], the EEL spectra are isotropic in the optical limit (see Fig. S7(b)). At $\mathbf{Q} \to 0$, the theoretical EEL spectra can reproduce the two prominent peaks, labelled A and B, in the experimental spectra. However, the discrepancy between the theoretical and experimental spectra in the higher energy window is noticeable, which could stem from the fact that the zero momentum transfer can never be achieved in the experiments [29, 35, 39], while we can directly set it to be zero in the theoretical calculations. This discrepancy is resolved for finite **Q** as shown in Fig. 5, where the theoretical spectra can accurately reproduce the experimental spectra.

We derive the EELS peak dispersion curves by monitoring the positions of peaks in the EEL spectra at different momentum transfers. Figure 6(c) shows the dispersion curves of the A and B peaks derived from the EEL spectra, alongside the experimental dispersion curves taken from Ref. [29]. Like the exciton band structure, we fit the A and B EELS peak dispersion relations with a third-order polynomial (green line). We choose the direction of fitting to be Γ M, and the fitting range spans $Q = 0.15 \text{ Å}^{-1}$ (about 8 % of the size of Brillouin zone). Within the range of fitting, the third-order poly-

^b Reference [28]

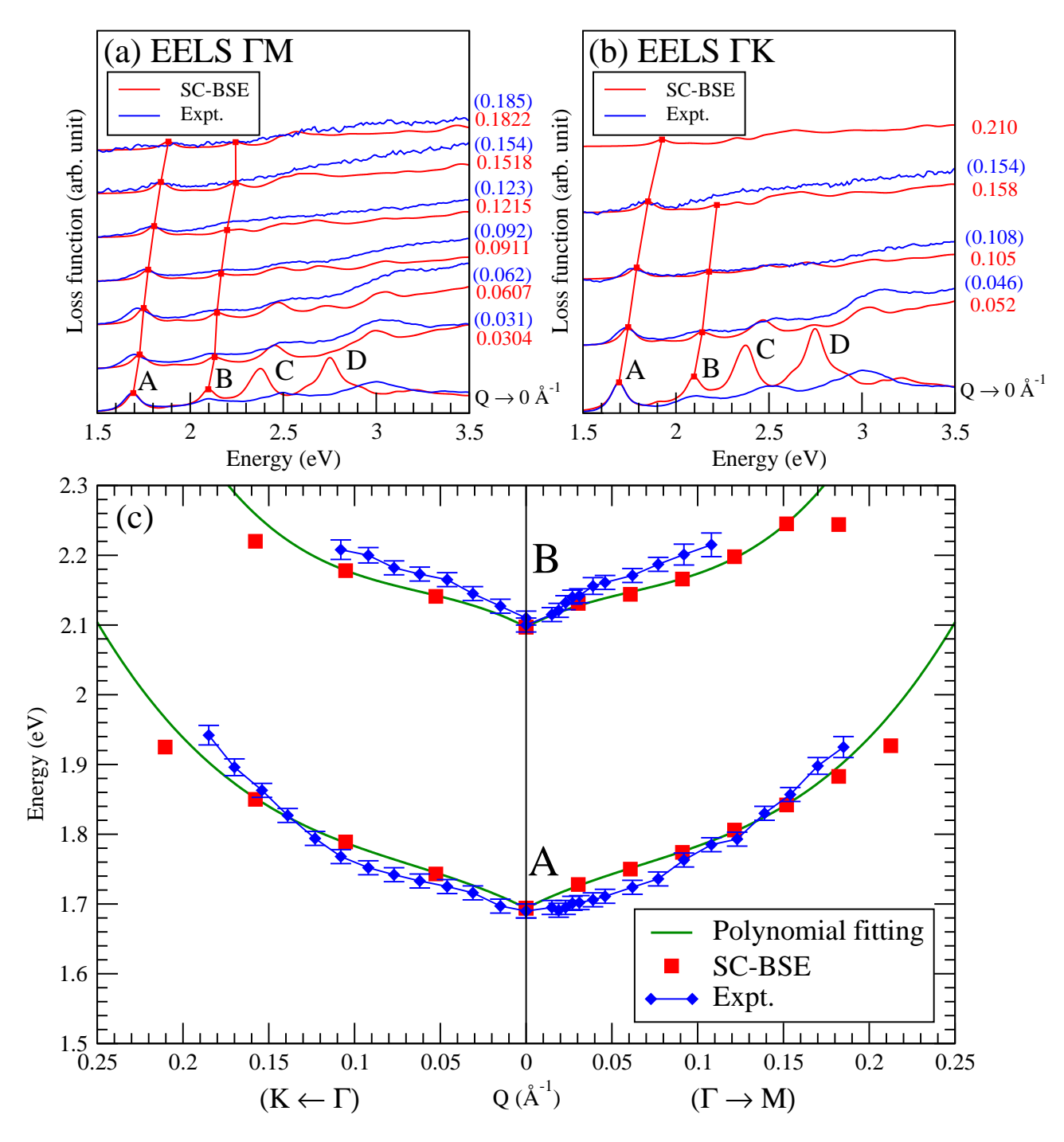


FIG. 6. The momentum-dependent EEL spectra of the WSe₂ monolayer along (a) Γ M and (b) Γ K directions obtained within the SC-BSE framework (red) and experimental measurement (blue) [29]. The corresponding EELS peaks at $\mathbf{Q} \to 0$ are labeled, and the theoretical A and B exciton peak dispersions are indicated by red squares connected with red lines, serving as a guild for clarity. The theoretical spectra have been normalized based on the experimental A exciton peak intensities. (c) The positions of the A and B EELS peaks along Γ M and Γ K directions (red squares). We simulate the A and B EELS peak dispersion curves by fitting in Γ M direction with a third-order polynomial (green line). The experimental EELS peak dispersion curves with error bars (blue diamonds) [29] are also shown for comparison.

nomial gives a good description of the dispersion curves for both A and B peaks, and the EELS peaks in the Γ K direction align closely with the fitting curves, indicating these peak dispersion curves are isotropic. Our

A and B EELS dispersion curves agree well with the experimental measurements in both ΓM and ΓK directions. Interestingly, as shown in Fig. 4, our A EELS dispersion curve follows the upper band of the A exciton and thus

exhibits a non-parabolic behavior. However, it is concluded in Ref. [29] that the A EELS dispersion curves are isotropic and parabolic in both ΓM and ΓK directions. Despite this, we note that the experimental A EELS dispersion can be interpreted as either parabolic or non-parabolic within the error bars of the experiment [29]. Therefore, the qualitative behavior of the A EELS dispersion curve remains an open question. On the other hand, both experimental and theoretical B EELS dispersion curves clearly manifest non-parabolic behavior. In the next section, we will explain why the EELS peaks should follow the upper band of the A exciton and thus show the non-parabolic dispersion behavior.

2. Selective excitation of excitons via EELS

To find the origin of the non-parabolic dispersion of the A exciton peaks, we show in Fig. 4 the dispersion curves of the A EELS peaks obtained within the SC-BSE framework (red squares) on top of the exciton band structure (black dots). Although numerous exciton states are within the energy range depicted in Fig. 4, not all of them contribute to the EEL spectrum. For example, the two lowest-energy dark excitons are not dipole-allowed and are therefore not visible in the EEL spectrum. Surprisingly, we find the calculated A EELS peaks unambiguously track the non-parabolic upper band of the A exciton, whereas the parabolic lower band does not contribute to the EEL spectrum. To understand the principles governing the electronic excitation mechanism in electron energy-loss spectroscopy, we analyze the definition of the EEL spectrum in Eq. (17). Based on firstorder $\mathbf{Q} \cdot \mathbf{p}$ perturbation theory [25, 30], and keeping terms up to the lowest order in \mathbf{Q} , the contribution from an exciton state $|\lambda\rangle$ to the EEL spectrum is

$$\left| \sum_{vc\mathbf{k}} A_{vc\mathbf{k}}^{\lambda,\mathbf{Q}} \rho_{vc\mathbf{k}}(\mathbf{Q}, 0) \right|^{2} \approx \left| \mathbf{Q} \cdot \frac{\hbar}{m} \sum_{\mathbf{k}} A_{vc\mathbf{k}}^{\lambda,0} \frac{\langle u_{v\mathbf{k}} | \mathbf{p} | u_{c\mathbf{k}} \rangle}{E_{cd^{-}}^{\mathrm{QP}} - E_{cd^{-}}^{\mathrm{QP}}} \right|^{2} = \left| \frac{\hbar}{m} \mathbf{Q} \cdot \mathbf{P}_{\lambda} \right|^{2}.$$
(30)

That is, the contribution of an exciton to the EEL spectrum is directly related to the inner product of its center-of-mass momentum and dipole matrix element of the exciton. Since our focus is primary on the in-plane momentum transfers (i.e., $\mathbf{Q} = \mathbf{Q}_{||}$), this indicates that the electron-energy-loss spectroscopy will selectively probe longitudinal excitons, while transverse excitons will have negligible contribution to the EEL spectrum. Remarkably, the non-parabolic upper band of the A exciton consists of longitudinal excitons, while the parabolic lower band of the A exciton comprises transverse excitons [28, 52]. Therefore, the A EELS peaks derived from the EEL spectrum will follow the non-parabolic upper band of the A exciton. Same argument can be applied to the dispersion of the B EELS peaks because the B exciton

bands will also split into the non-parabolic upper band and the parabolic lower band at finite \mathbf{Q} [28], with the upper (lower) band consists of the longitudinal (transverse) excitons [28]. We note that this argument is not exclusive to the WSe₂ monolayer. Instead, it can be considered the signature of quasi-2D materials.

Next, we provide an alternative perspective on this phenomenon. The EELS techniques exploit swift electrons that interact with a specimen to unravel its underlying excitation, such as plasmon and exciton [29, 39]. Considering an electron moving along the z axis with velocity v, here z is the direction perpendicular to the quasi-2D sheet, and the total momentum transfer of the electron \mathbf{Q} consists of its in-plane component $\mathbf{Q}_{||}$ and out-of-plane component $q_z \hat{\mathbf{z}}$. The electric field produced by it in vacuum is [39]

$$\mathbf{E}(\mathbf{r},\omega) = \frac{ie}{\pi} \int d^3 \mathbf{Q} \frac{\mathbf{Q} - \frac{\omega}{c^2} \mathbf{v}}{|\mathbf{Q}|^2 - \frac{\omega^2}{c^2}} e^{i\mathbf{Q} \cdot \mathbf{r}} \delta(\omega - \mathbf{Q} \cdot \mathbf{v}). \quad (31)$$

By performing the in-plane Fourier transform on the electric field, the Fourier coefficient of the electric field can be decomposed into the in-plane component

$$E_{||}(\mathbf{Q}_{||}) = \frac{ie}{\pi} \frac{e^{i\frac{\omega}{\nu}z}}{|\mathbf{Q}_{||}|^2 + \frac{\omega^2}{\nu^2}(1 - \frac{v^2}{c^2})} \mathbf{Q}_{||}$$
(32)

and the out-of-plane component

$$E_z(\mathbf{Q}_{||}) = \frac{ie}{\pi} \frac{e^{i\frac{\omega}{v}z}}{\left|\mathbf{Q}_{||}\right|^2 + \frac{\omega^2}{v^2}(1 - \frac{v^2}{c^2})} (1 - \frac{v^2}{c^2}) q_z \hat{\mathbf{z}}.$$
 (33)

We derive Eq. (32) and Eq. (33) in supplementary note 4 [61]. Interestingly, the in-plane component and out-of-plane component are proportional and parallel to $\mathbf{Q}_{||}$ and $q_z \hat{\mathbf{z}}$, respectively.

In the previous experimental setup [29], the incident electron was moving in the out-of-plane (z) direction. Due to the high velocity of the incident electrons, the magnitude of q_z is considerably smaller than that of $\mathbf{Q}_{||}$ [29, 39]. That is, the electric field primarily lies in-plane, which is parallel to $\mathbf{Q}_{||}$. The electric field then probe an exciton with its exciton dipole matrix element in the direction of $\mathbf{Q}_{||}$, which is exactly the center-of-mass momentum of this exciton. This coincides with the definition of a longitudinal exciton, explaining that the EELS will only selectively probe the longitudinal exciton consisting of the upper band of the A and B exciton under this experimental setup.

It will also be interesting to probe the other exciton bands, such as the lower parabolic band of the A and B exciton using EELS techniques. Given that the lower parabolic band of the A and B exciton consists of the transverse exciton with its exciton dipole matrix element pointing to the z direction [28], we consider the electric field from incident electrons at a specific momentum transfer also pointing primarily in the z direction, which can be achieved by rotating the direction of the incident

electron beam to the x axis. In this case, the Fourier component of the electric field in the x direction will be small compared to its y component

$$E_y(Q_y, Q_z) = \frac{ie}{\pi} \frac{e^{i\frac{\omega}{v}x}}{(Q_y^2 + Q_z^2) + \frac{\omega^2}{v^2}(1 - \frac{v^2}{c^2})} Q_y \qquad (34)$$

and the z component

$$E_z(Q_y, Q_z) = \frac{ie}{\pi} \frac{e^{i\frac{\omega}{v}x}}{(Q_y^2 + Q_z^2) + \frac{\omega^2}{v^2}(1 - \frac{v^2}{c^2})} Q_z.$$
 (35)

By choosing a momentum transfer with $Q_z > Q_y \gg q_x = \omega/v$, the electric field will lie primarily in the z direction to couple with the exciton polarization, while the motion of the exciton is constrained to the x-y plane due to the monolayer structure. Therefore, we can probe the lower band of the A and B exciton consisting of the transverse exciton in this experimental setup. However, it should be noted that the derived formula of Eq. (25) is only valid for the transmission EELS with the direction of the incident electron beam along the z-axis.

V. CONCLUSIONS

In summary, we have carefully studied the different EEL spectrum formulas for quasi-2D materials that have been widely used in the literature, and established an appropriate definition of the EEL spectrum, a formula adopted in many previous studies yet lacking a clear explanation until now. By utilizing the state-of-the art ab initio BSE calculations with the relativistic spin-orbit coupling included, we have investigated the excitons with finite center-of-mass momentum (i.e., exciton band structure) and, with the proper EELS formula mentioned above, have also calculated the EEL spectrum of the WSe₂ monolayer with a perpendicular incident electron beam, as in the previous experimental setup [29]. We identify five exciton states through the calculated optical

absorbance of the WSe₂ monolayer, including the lowestenergy bright A exciton. Our theoretical analysis reveals that due to the electron-hole exchange interaction, the bright A exciton bands which are degenerate at the zero momentum transfer Q = 0, split at finite momentum transfers. The lower branch of the A exciton and also the dark exciton bands exhibit parabolic characteristics, while the upper band of the A exciton shows a nonparabolic dispersion relation. Interestingly, the dispersion of the calculated lowest-energy EELS peaks follows closely the non-parabolic upper band of the A exciton, and also agrees well with the experimental spectrum in the low-energy-loss regime [29]. Furthermore, our analysis also shows that EELS experiments would selectively probe those exciton bands having their dipole being parallel to the transferred momentum. This explains why only the upper band of the A exciton, which is a longitudinal exciton with an in-plane dipole moment, was observed in the previous experiment [29]. Our findings thus suggest further EELS experiments with different orientations of the incident electron beam to measure other branches, such as the parabolic lower band of the A exciton, of the exciton band structure and hence to gain a full understanding of the exciton dynamics in quasi-2D materials.

VI. ACKNOWLEDGMENTS

The authors would like to express their gratitude to the authors of [29] for generously sharing their digital data of the experimental EEL spectra with us. Y.-C.S and G.-Y.G thank the support from the National Science and Technology Council and National Center for Theoretical Sciences (NCTS), Taiwan. F.N has received funding from the European Union's Horizon 2020 research and innovation program under the Marie Skłodowska-Curie grant agreement No. 899987. (EuroTechPostdoc2). Fruitful discussions with K. S. Thygesen, M. Ohm Sauer and T. G. Pedersen are also gratefully acknowledged.

Z. Y. Zhu, Y. C. Cheng, and U. Schwingenschlögl, Giant spin-orbit-induced spin splitting in two-dimensional transition-metal dichalcogenide semiconductors, Phys. Rev. B 84, 153402 (2011).

^[2] M. Chhowalla, H. S. Shin, G. Eda, L.-J. Li, K. P. Loh, and H. Zhang, The chemistry of two-dimensional layered transition metal dichalcogenide nanosheets, Nat. Chem. 5, 263 (2013).

^[3] W. Zhao, Z. Ghorannevis, L. Chu, M. Toh, C. Kloc, P.-H. Tan, and G. Eda, Evolution of Electronic Structure in Atomically Thin Sheets of WS₂ and WSe₂, ACS Nano 7, 791 (2013).

^[4] G. Sallen, L. Bouet, X. Marie, G. Wang, C. R. Zhu, W. P. Han, Y. Lu, P. H. Tan, T. Amand, B. L. Liu, and B. Urbaszek, Robust optical emission polarization

in $\rm MoS_2$ monolayers through selective valley excitation, Phys. Rev. B $\bf 86,\,081301(R)$ (2012).

^[5] D. Xiao, G.-B. Liu, W. Feng, X. Xu, and W. Yao, Coupled Spin and Valley Physics in Monolayers of MoS₂ and Other Group-VI Dichalcogenides, Phys. Rev. Lett. 108, 196802 (2012).

^[6] T. Cao, G. Wang, W. Han, H. Ye, C. Zhu, J. Shi, Q. Niu, P. Tan, E. Wang, B. Liu, and J. Feng, Valley-selective circular dichroism of monolayer molybdenum disulphide, Nat. Commun. 3, 887 (2012).

^[7] H. Zeng, J. Dai, W. Yao, D. Xiao, and X. Cui, Valley polarization in MoS₂ monolayers by optical pumping, Nat. Nanotechnol 7, 490 (2012).

^[8] K. F. Mak, K. He, J. Shan, and T. F. Heinz, Control of valley polarization in monolayer MoS₂ by optical helicity,

- Nat. Nanotechnol 7, 494 (2012).
- [9] L. V. Keldysh, Coulomb interaction in thin semiconductor and semimetal films, JETP Lett. **29**, 658 (1979).
- [10] P. Cudazzo, I. V. Tokatly, and A. Rubio, Dielectric screening in two-dimensional insulators: Implications for excitonic and impurity states in graphane, Phys. Rev. B 84, 085406 (2011).
- [11] F. Hüser, T. Olsen, and K. S. Thygesen, How dielectric screening in two-dimensional crystals affects the convergence of excited-state calculations: Monolayer MoS₂, Phys. Rev. B 88, 245309 (2013).
- [12] S. Latini, T. Olsen, and K. S. Thygesen, Excitons in van der Waals heterostructures: The important role of dielectric screening, Phys. Rev. B 92, 245123 (2015).
- [13] X. L. Yang, S. H. Guo, F. T. Chan, K. W. Wong, and W. Y. Ching, Analytic solution of a two-dimensional hydrogen atom. I. Nonrelativistic theory, Phys. Rev. A 43, 1186 (1991).
- [14] A. Ramasubramaniam, Large excitonic effects in monolayers of molybdenum and tungsten dichalcogenides, Phys. Rev. B 86, 115409 (2012).
- [15] D. Y. Qiu, F. H. da Jornada, and S. G. Louie, Optical Spectrum of MoS₂: Many-Body Effects and Diversity of Exciton States, Phys. Rev. Lett. 111, 216805 (2013).
- [16] A. Chernikov, T. C. Berkelbach, H. M. Hill, A. Rigosi, Y. Li, B. Aslan, D. R. Reichman, M. S. Hybertsen, and T. F. Heinz, Exciton Binding Energy and Nonhydrogenic Rydberg Series in Monolayer WS₂, Phys. Rev. Lett. 113, 076802 (2014).
- [17] K. He, N. Kumar, L. Zhao, Z. Wang, K. F. Mak, H. Zhao, and J. Shan, Tightly Bound Excitons in Monolayer WSe₂, Phys. Rev. Lett. 113, 026803 (2014).
- [18] K. F. Mak, C. Lee, J. Hone, J. Shan, and T. F. Heinz, Atomically Thin MoS₂: A New Direct-Gap Semiconductor, Phys. Rev. Lett. 105, 136805 (2010).
- [19] Y. Li, A. Chernikov, X. Zhang, A. Rigosi, H. M. Hill, A. M. Van Der Zande, D. A. Chenet, E. M. Shih, J. Hone, and T. F. Heinz, Measurement of the optical dielectric function of monolayer transition-metal dichalcogenides: MoS₂, MoSe₂, WS₂, and WSe₂, Phys. Rev. B **90**, 205422 (2014).
- [20] Q. H. Wang, K. Kalantar-Zadeh, A. Kis, J. N. Coleman, and M. S. Strano, Electronics and optoelectronics of twodimensional transition metal dichalcogenides, Nat. Nanotechnol 7, 699 (2012).
- [21] K. F. Mak and J. Shan, Photonics and optoelectronics of 2D semiconductor transition metal dichalcogenides, Nat. Nanotechnol 10, 216 (2016).
- [22] X.-X. Zhang, Y. You, S. Y. F. Zhao, and T. F. Heinz, Experimental Evidence for Dark Excitons in Monolayer WSe₂, Phys. Rev. Lett. 115, 257403 (2015).
- [23] M. Selig, G. Berghäuser, M. Richter, R. Bratschitsch, A. Knorr, and E. Malic, Dark and bright exciton formation, thermalization, and photoluminescence in monolayer transition metal dichalcogenides, 2D Mater. 5, 035017 (2018).
- [24] F. Wu, F. Qu, and A. H. MacDonald, Exciton band structure of monolayer MoS₂, Phys. Rev. B 91, 075310 (2015).
- [25] D. Y. Qiu, T. Cao, and S. G. Louie, Valley Quantum Phases, and Lightlike Exciton Dispersion in Monolayer Transition Metal Dichalcogenides: Theory and First-Principles Calculations, Phys. Rev. Lett. 115, 176801 (2015).

- [26] P. Cudazzo, L. Sponza, C. Giorgetti, L. Reining, F. Sottile, and M. Gatti, Exciton Band Structure in Two-Dimensional Materials, Phys. Rev. Lett. 116, 066803 (2016).
- [27] T. Deilmann and K. S. Thygesen, Finite-momentum exciton landscape in mono- and bilayer transition metal dichalcogenides, 2D Mater. 6, 035003 (2019).
- [28] M. O. Sauer, C. E. M. Nielsen, L. Merring-Mikkelsen, and T. G. Pedersen, Optical emission from light-like and particle-like excitons in monolayer transition metal dichalcogenides, Phys. Rev. B 103, 205404 (2021).
- [29] J. Hong, R. Senga, T. Pichler, and K. Suenaga, Probing Exciton Dispersions of Freestanding Monolayer WSe₂ by Momentum-Resolved Electron Energy-Loss Spectroscopy, Phys. Rev. Lett. 124, 087401 (2020).
- [30] D. Y. Qiu, G. Cohen, D. Novichkova, and S. Refaely-Abramson, Signatures of Dimensionality and Symmetry in Exciton Band Structure: Consequences for Exciton Dynamics and Transport, Nano Lett. 21, 7644 (2021).
- [31] K. Andersen and K. S. Thygesen, Plasmons in metallic monolayer and bilayer transition metal dichalcogenides, Phys. Rev. B 88, 155128 (2013).
- [32] S. C. Liou, C.-S. Shie, C. H. Chen, R. Breitwieser, W. W. Pai, G.-Y. Guo, and M.-W. Chu, π-plasmon dispersion in free-standing graphene by momentum-resolved electron energy-loss spectroscopy, Phys. Rev. B 91, 045418 (2015).
- [33] H. C. Nerl, K. T. Winther, F. S. Hage, K. S. Thygesen, L. Houben, C. Backes1, J. N. Coleman1, Q. M. Ramasse, and V. Nicolosi, Probing the local nature of excitons and plasmons in few-layer MoS₂, npj 2D Mater. Appl. 1, 2 (2017).
- [34] J. Hong, M. K. Svendsen, M. Koshino, T. Pichler, H. Xu, K. Suenaga, and K. S. Thygesen, Momentum-Dependent Oscillator Strength Crossover of Excitons and Plasmons in Two-Dimensional PtSe₂, ACS Nano 16, 12328 (2022).
- [35] J. Hong, M. Koshino, R. Senga, T. Pichler, H. Xu, and K. Suenaga, Deciphering the Intense Postgap Absorptions of Monolayer Transition Metal Dichalcogenides, ACS Nano 15, 7783 (2021).
- [36] K. Sturm, Electron energy loss in simple metals and semiconductors, Adv. Phys. 31, 1 (1982).
- [37] J. Yan, J. J. Mortensen, K. W. Jacobsen, and K. S. Thygesen, Linear density response function in the projector augmented wave method: Applications to solids, surfaces, and interfaces, Phys. Rev. B 83, 245122 (2011).
- [38] C. Habenicht, M. Knupfer, and B. Büchner, Investigation of the dispersion and the effective masses of excitons in bulk 2H MoS₂ using transition electron energy-loss spectroscopy, Phys. Rev. B 91, 245203 (2015).
- [39] F. J. García de Abajo, Optical excitations in electron microscopy, Rev. Mod. Phys. 82, 209 (2010).
- [40] K. Sturm, Dynamic Structure Factor: An Introduction, Z. Naturforsch. 48a, 233 (1993).
- [41] V. U. Nazarov, Electronic excitations in quasi-2D crystals: what theoretical quantities are relevant to experiment?, New Journal of Physics 17, 073018 (2015).
- [42] J. J. Mortensen, A. H. Larsen, M. Kuisma, A. V. Ivanov, A. Taghizadeh, A. Peterson, A. Haldar, A. O. Dohn, C. Schäfer, E. Orn Jónsson, E. D. Hermes, F. A. Nilsson, G. Kastlunger, G. Levi, H. Jónsson, H. Häkkinen, J. Fojt, J. Kangsabanik, J. Sødequist, J. Lehtomäki et al., GPAW: An open Python package for electronic structure calculations, J. Chem. Phys. 160, 092503 (2024).

- [43] J. Enkovaara, C. Rostgaard, J. J. Mortensen, J. Chen, M. Du lak, L. Ferrighi, J. Gavnholt, C. Glinsvad, V. Haikola, H. A. Hansen, H. H. Kristoffersen, M. Kuisma, A. H. Larsen, L. Lehtovaara, M. Ljungberg, O. Lopez-Acevedo, P. G. Moses, J. Ojanen, T. Olsen, V. Petzold et al., Electronic structure calculations with GPAW: a real-space implementation of the projector augmentedwave method, J. Phys. Condens. Matter 22, 253202 (2010).
- [44] A. H. Larsen, J. J. Mortensen, J. Blomqvist, I. E. Castelli, R. Christensen, M. Du lak, J. Friis, M. N. Groves, B. Hammer, C. Hargus, E. D. Hermes, P. C. Jennings, P. B. Jensen, J. Kermode, J. R. Kitchin, E. L. Kolsbjerg, J. Kubal, K. Kaasbjerg, S. Lysgaard, J. B. Maronsson et al., The atomic simulation environment—a Python library for working with atoms, J. Phys. Condens. Matter 29, 273002 (2017).
- [45] J. J. Mortensen, L. B. Hansen, and K. W. Jacobsen, Real-space grid implementation of the projector augmented wave method, Phys. Rev. B 71, 035109 (2005).
- [46] J. P. Perdew, K. Burke, and M. Ernzerhof, Generalized Gradient Approximation Made Simple, Phys. Rev. Lett. 77, 3865 (1996).
- [47] F. Hüser, T. Olsen, and K. S. Thygesen, Quasiparticle GW calculations for solids, molecules, and two-dimensional materials, Phys. Rev. B 87, 235132 (2013).
- [48] F. A. Rasmussen, P. S. Schmidt, K. T. Winther, and K. S. Thygesen, Efficient many-body calculations for two-dimensional materials using exact limits for the screened potential: Band gaps of MoS₂, h-BN, and phosphorene, Phys. Rev. B **94**, 155406 (2016).
- [49] M. Rohlfing and S. G. Louie, Electron-hole excitations and optical spectra from first principles, Phys. Rev. B 62, 4927 (2000).
- [50] J. Yan, K. W. Jacobsen, and K. S. Thygesen, Optical properties of bulk semiconductors and graphene/boron nitride: The Bethe-Salpeter equation with derivative discontinuity-corrected density functional energies, Phys. Rev. B 86, 045208 (2012).
- [51] G. Onida, L. Reining, and A. Rubio, Electronic excitations: density-functional versus many-body Green's-function approaches, Rev. Mod. Phys. 74, 601 (2002).
- [52] M. M. Denisov and V. P. Makarov, Longitudinal and Transverse Excitons in Semiconductors, Phys. Status Solidi B 56, 9 (1973).
- [53] C. A. Rozzi, D. Varsano, A. Marini, E. K. U. Gross, and A. Rubio, Exact Coulomb cutoff technique for supercell calculations, Phys. Rev. B 73, 205119 (2006).
- [54] S. Ismail-Beigi, Truncation of periodic image interactions for confined systems, Phys. Rev. B 73, 233103 (2006).
- [55] J. Fink, Recent Developments in Energy-Loss Spectroscopy Adv. Electron. Electron Phys. 75, 121 (1989).
- [56] P. Johari and V. B. Shenoy, Tunable Dielectric Properties of Transition Metal Dichalcogenides, ACS Nano 5, 5903 (2011).

- [57] X. W. Zhao, Z. Yang, J. T. Guo, G. C. Hu, W. W. Yue, X. B. Yuan, and J. F. Ren, Tuning electronic and optical properties of monolayer PdSe₂ by introducing defects: first-principles calculations, Sci. Rep. 10, 4028 (2020).
- [58] G. Yang, J. Fan, and S.-P. Gao, Momentum and thickness dependent excitonic and plasmonic properties of 2D h-BN and MoS₂ restored from supercell calculations, Nanoscale Adv. 5, 6990 (2023).
- [59] K. S. Thygesen, Calculating excitons, plasmons, and quasiparticles in 2D materials and van der Waals heterostructures, 2D Mater. 4, 022004 (2017).
- [60] Z. Yuan and S. Gao, Linear response approach to collective electronic excitations of solids and surfaces, Comput. Phys. Commun. 180, 466 (2009).
- [61] See Supplemental Material at http://link.aps.org/supplemental/ for supplementary Notes 1-4, Figs. S1-S7, and Tables S1-S6, which also includes Ref. [62].
- [62] N. W. Ashcroft, and N. D. Mermin, Solid State Physics (Harcourt College Publishers, 1976).
- [63] C. Zhang, Y. Chen, A. Johnson, M.-Y. Li, L.-J. Li, P. C. Mende, R. M. Feenstra, and C.-K. Shih, Probing Critical Point Energies of Transition Metal Dichalcogenides: Surprising Indirect Gap of Single Layer WSe₂, Nano Lett. 15, 6494 (2015).
- [64] Y. Zhang, M. M. Ugeda, C. Jin, S.-F. Shi, A. J. Bradley, A. Martín-Recio, H. Ryu, J. Kim, S. Tang, Y. Kim, B. Zhou, C. Hwang, Y. Chen, F. Wang, M. F. Crommie, Z. Hussain, Z.-X. Shen, and S.-K. Mo, Electronic Structure, Surface Doping, and Optical Response in Epitaxial WSe₂ Thin Films, Nano Lett. 16, 2485 (2016).
- [65] D. Le, A. Barinov, E. Preciado, M. Isarraraz, I. Tanabe, T. Komesu, C. Troha, L. Bartels, T. S. Rahman, and P. A. Dowben, Spin-orbit coupling in the band structure of monolayer WSe₂, J. Phys. Condens. Matter 27, 182201 (2015).
- [66] P. Kapuściński, A. Delhomme, D. Vaclavkova, A. O. Slobodeniuk, M. Grzeszczyk, M. Bartos, K. Watanabe, T. Taniguchi, C. Faugeras, and M. Potemski, Rydberg series of dark excitons and the conduction band spin-orbit splitting in monolayer WSe₂, Commun. Phys. 4, 186 (2021).
- [67] L. Ren, C. Robert, H. Dery, M. He, P. Li, D. V. Tuan, P. Renucci, D. Lagarde, T. Taniguchi, K. Watanabe, X. Xu, and X. Marie, Measurement of the conduction band spin-orbit splitting in WSe₂ and WS₂ monolayers, Phys. Rev. B 107, 245407 (2023).
- [68] M. Drüppel, T. Deilmann, J. Noky, P. Marauhn, P. Krüger, and M. Rohlfing, Electronic excitations in transition metal dichalcogenide monolayers from an LDA + GdW approach, Phys. Rev. B 98, 155433 (2018).
- [69] W.-T. Hsu, L.-S. Lu, D. Wang, J.-K. Huang, M.-Y. Li, T.-R. Chang, Y.-C. Chou, Z.-Y. Juang, H.-T. Jeng, L.-J. Li, and W.-H. Chang, Evidence of indirect gap in monolayer WSe₂, Nat. Commun. 8, 929 (2017).
- [70] B. Aslan, M. Deng, and T. F. Heinz, Strain tuning of excitons in monolayer WSe₂, Phys. Rev. B 98, 115308 (2018).